Continuum-electron interferometry for enhancement of photoelectron circular dichroism and measurement of bound, free, and mixed contributions to chiral response

R. Esteban Goetz,[1,*] Alexander Blech,[2] Corbin Allison,[1] Christiane P. Koch,[2] and Loren Greenman[1,†]

[1] *J. R. Macdonald Laboratory, Department of Physics, Kansas State University, Manhattan, KS 66506*
[2] *Dahlem Center for Complex Quantum Systems and Fachbereich Physik, Freie Universität Berlin, Arnimallee 14, D-14195 Berlin, Germany*

(Dated: December 18, 2023)

We develop photoelectron interferometry based on laser-assisted extreme ultraviolet ionization for flexible and robust control of photoelectron circular dichroism in randomly oriented chiral molecules. A comb of XUV photons ionizes a sample of chiral molecules in the presence of a time-delayed infrared or visible laser pulse promoting interferences between components of the XUV-ionized photoelectron wave packet. In striking contrast to multicolor phase control schemes relying on pulse shaping techniques, the magnitude of the resulting chiral signal is here controlled by the time delay between the XUV and laser pulses. Furthermore, we show that the relative polarization configurations of the XUV and IR fields allows for disentangling the contributions of bound and continuum states to the chiral response. Our proposal provides a simple, robust and versatile tool for the control of photoelectron circular dichroism and experimentally feasible protocol for probing the individual contributions of bound and continuum states to the PECD in a time-resolved manner.

Chirality, the property of a molecule to be non-superposable with its mirror image [1], is a ubiquitous property in nature with profound effects on many fundamental chemical and physical processes. Photoelectron circular dichroism (PECD) is a signature of chirality and designates the relatively strong effect whereby randomly oriented chiral molecules ionize asymmetrically for left- and right-circularly polarized light [2]. The strength of PECD has led to its use to observe chirality in molecules [3–20] and turned it into a practical tool for, e.g., measuring enantiomeric excess [6, 17, 18]. Techniques to enhance the PECD in chiral molecules include time-resolved pump-probe photoexcitation circular dichroism [17], coherent control of PECD in bichromatic [21, 22] and resonantly-enhanced multiphoton ionization [23], as well as use of a continuum resonance and Fano interference [24]. While these techniques focus on maximizing the PECD signal, the relative contribution of bound and continuum states to the PECD has not yet been addressed, and none of these approaches have been shown to disentangle the contributions of bound and continuum states in a systematic way. Furthermore, schemes that show high enhancements of the PECD such as the shaped resonantly-enhanced multiphoton ionization (REMPI) pulses we have previously suggested [23] require challenging generation of and control over the spectral coherence of multicolor ultraviolet laser fields.

In this letter, we propose a flexible, yet robust, photoelectron interferometry approach to probe bound and continuum contributions to PECD in randomly oriented molecules. Our method has the advantage over that of Ref. [23] that it does not require shaping circularly polarized XUV laser sources, a formidable experimental challenge. Rather, it relies on an adaptation of the RABBITT (reconstruction of attosecond beating by interference of two-photon transitions) technique [25, 26], a versatile interferometric approach which has been implemented in many experimental laboratories [27–29]. The necessary circularly polarized XUV fields have been synthesized [30, 31] and used in PECD experiments recently [32]. A variant of RABBITT called CHABBIT, a laser-assisted, self-referenced, above-threshold ionization attosecond photoelectron interferometry has been used to extract the temporal profile and phase difference in the photoelectron emission in chiral molecules along different directions [16]. Here, we suggest to directly probe the individual contributions of bound and continuum states and their interference to the PECD. We show how changing the polarization configurations of the XUV and IR fields results in different asymmetries in the photoelectron angular distributions in randomly oriented chiral molecules.

Using CHBrClF as a prototypical chiral molecule [33, 34], we explain how promoting interferences in the continuum in a controlled manner results in precise control of PECD after XUV ionization in the presence of a time-delayed IR field. Rather than relying on multiple resonantly enhanced multiphoton ionization and multicolor pulse shaping techniques to control PECD [23], control here is achieved by adjusting the time delay between the XUV comb and IR field or by varying the IR pulse duration. Changing the polarization configuration of the pulses with optimized delay and IR duration allows for revealing the chiral contributions of different states.

The photoionization dynamics is described within the fixed-nuclei and nonrelativistic dipole approximations. The time-dependent Schrödinger equation reads

$$i\frac{\partial}{\partial t}|\Psi^N_{\gamma_\mathcal{R}}(t)\rangle = \left[\hat{\mathsf{H}}_0 - \sum_{\mu,\mu'}\mathcal{D}^{(1)*}_{\mu,\mu'}(\gamma_\mathcal{R})\,\mathrm{E}_{\mu'}(t)\,\hat{\mathsf{r}}_\mu\right]|\Psi^N_{\gamma_\mathcal{R}}(t)\rangle\,, \tag{1a}$$

with $\hat{\mathsf{H}}_0$ the field-free Hamiltonian, $\gamma_{\mathcal{R}}$ the Euler angles defining the orientation of the molecular frame, $\mathcal{R}$, with respect to the laboratory frame $\mathcal{R}'$, $\mathcal{D}^{(1)}_{\mu,\mu'}(\gamma_{\mathcal{R}})$ the elements of the Wigner rotation matrix, $\mathrm{E}_\mu(t)$ the electric field component along the spherical unit vector $\mathbf{e}_\mu$, with $\mu = \pm 1, 0$, and finally, $\hat{\mathsf{r}}_\mu$ the component of the position operator in the direction of $\mathbf{e}_\mu$. In $\mathcal{R}'$, the electric field is a superposition of an XUV comb and an IR, resp. visible, field,

$$\mathbf{E}(t) = \sum_k^{N_p} \mathbf{E}_k^{(\mathrm{XUV})}(t) + \mathbf{E}^{(\mathrm{IR/VIS})}(t - \tau_{\mathrm{IR/VIS}})\,, \tag{1b}$$

with

$$\mathbf{E}_k^{(\mathrm{XUV})}(t) = h_k(t-\tau_k)\mathrm{Re}\left\{\mathrm{E}_{k,0}\, e^{-i(\omega_k(t-\tau_k)+\tilde{\phi}_k)}\,\mathbf{e}_{\mathrm{XUV}}\right\},$$

where $k = 2q+1$ with q an integer, i.e., the XUV frequencies are odd multiples of the fundamental ω_0 such that $\omega_{2q+1} = (2q+1)\omega_0$. $h_k(\cdot)$ is a Gaussian function and $\mathbf{e}_{\mathrm{XUV}}$ the covariant spherical unit vector describing circularly left ($\mathbf{e}_{-1} = (\mathbf{e}_x - i\mathbf{e}_y)/\sqrt{2}$), right ($\mathbf{e}_{+1} = -(\mathbf{e}_x + i\mathbf{e}_y)/\sqrt{2}$) and linear ($\mathbf{e}_0 = \mathbf{e}_z$) polarization of the radiation field. Note that τ_k describes the inherent chirp if the various XUV components are temporally delayed [35, 36]. IR and visible pulses are analogously defined with $h_{\mathrm{IR/VIS}}(t - \tau_{\mathrm{IR/VIS}})$ and $\omega_{\mathrm{IR/VIS}}$, and $\tau_{\mathrm{IR/VIS}}$ describes the delay between the IR/VIS and XUV field.

In the following, we explore two cases. First, the frequency ω_{IR} is identical with the fundamental ω_0 ($\omega_{\mathrm{IR}} = \omega_0 = 1.5\,\mathrm{eV}$) to control PECD at the sidebands, cf. Fig. 5(a). Second, the frequency is twice the fundamental ($\omega_{\mathrm{VIS}} = 3.0\,\mathrm{eV}$) to control PECD at the harmonic peaks, cf. Fig. 7(a). The PECD is determined by the difference in the photoelectron angular distribution (PAD) obtained by reversing the helicity of the XUV, the IR, or both,

$$\mathrm{PECD}(\epsilon_k, \theta_{\boldsymbol{k}'}) = \frac{d^2\sigma(\mathbf{e}_{\mathrm{XUV}}, \mathbf{e}_{\mathrm{IR}})}{d\epsilon_k\, d\Omega_{\boldsymbol{k}'}} - \frac{d^2\sigma(\mathbf{e}'_{\mathrm{XUV}}, \mathbf{e}'_{\mathrm{IR}})}{d\epsilon_k\, d\Omega_{\boldsymbol{k}'}}\,. \tag{2}$$

Throughout, we report PECD in percentage of the mean peak intensity of the PADs obtained with polarization reversals [37]. Following Refs. [23, 38], the orientation-averaged photoelectron momentum distribution is obtained by calculating $|\Psi^N_{\gamma_{\mathcal{R}}}(t)\rangle$ within the time-dependent configuration interaction singles method and second-order time-dependent perturbation theory of the light-matter interaction. The differential photoionization cross section is then given by

$$\frac{d^2\sigma(\mathbf{e}_{\mathrm{XUV}}, \mathbf{e}_{\mathrm{IR}})}{d\epsilon_k\, d\Omega_{\boldsymbol{k}'}} \approx \int \left|\alpha^{\boldsymbol{k}'\,(1)}_{i_0}(\gamma_{\mathcal{R}}) + \alpha^{\boldsymbol{k}'\,(2)}_{i_0}(\gamma_{\mathcal{R}})\right|^2 \mathrm{d}^3\gamma_{\mathcal{R}}, \tag{3}$$

with $\alpha^{\boldsymbol{k}'\,(1,2)}_{i_0}(\gamma_{\mathcal{R}}) = \langle \Phi^{\boldsymbol{k}'}_{i_0} | \Psi^{N(1,2)}_{\gamma_{\mathcal{R}}}(t)\rangle$ the first, resp. second, order corrections for $t \to \infty$. The index i_0 refers to the contribution from the highest occupied molecular orbital (HOMO).

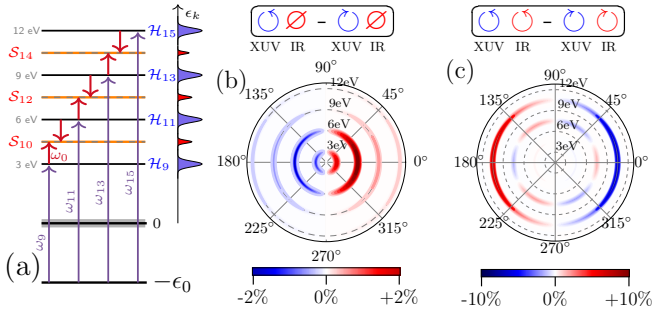

FIG. 1. (a) RABBITT scheme for measuring PECD, Eq. (2): An asymmetric photoelectron spectrum peaked at the harmonics $\mathcal{H}_{2q+1}$ is generated by single-photon ionization of a chiral molecule's ground state (with ionization potential ϵ_0), driven by an XUV comb with frequencies ω_{2q+1}, which are odd multiples of ω_0. In the presence of an IR field with mean photon energy $\omega_{\mathrm{IR}} = \omega_0$, portions of the photoelectron wave packet with energies $\mathcal{H}_{2q-1}$ and $\mathcal{H}_{2q+1}$ interfere, giving rise to sideband formation $\mathcal{S}_{2q}$. This interference can be used to modify the magnitude of PECD, seen most prominently when comparing PECD obtained with (c) and without (b) IR field.

The continuum states $|\Phi^{\boldsymbol{k}'}_{i_0}\rangle$, consisting of particle-hole excitations to the continuum orbitals $\varphi^-_{\boldsymbol{k}'}(\boldsymbol{r})$ with energies $k^2/2$ and direction of photoelectron emission $\Omega_{\boldsymbol{k}'} = (\theta_{\boldsymbol{k}'}, \phi_{\boldsymbol{k}'})$ in $\mathcal{R}'$ [39] are constructed from the anti-symmetrized product [40, 41]

$$\Phi^{\boldsymbol{k}'}_{i_0}(\boldsymbol{r}_1, \ldots \boldsymbol{r}_N) = \mathcal{A}_N\left[\varphi^-_{\boldsymbol{k}'}(\boldsymbol{r}); \Phi_{i_0}(\boldsymbol{r}_1, \ldots \boldsymbol{r}_{N-1})\right], \tag{4}$$

with $\Phi_{i_0}(\boldsymbol{r}_1, \ldots \boldsymbol{r}_{N-1})$ the ionic component and $\varphi^-_{\boldsymbol{k}'}(\mathbf{r})$ the photoelectron scattering wave function. The latter is obtained as a solution of the scattering problem [42],

$$\left[-\frac{\boldsymbol{\nabla}^2}{2} - \frac{1}{r} + V(\boldsymbol{r}) - \frac{k^2}{2}\right]\varphi^-_{\boldsymbol{k}}(\boldsymbol{r}) = 0\,, \tag{5a}$$

with $V(\boldsymbol{r})$ the short-range portion of the static-exchange potential [42]. The scattering states with momentum $\boldsymbol{k}'$ in the laboratory frame are obtained according to

$$\varphi^-_{\boldsymbol{k}'}(\boldsymbol{r}) = \sum_{\ell,m,m'} \varphi^-_{k,\ell,m}(\boldsymbol{r})\, \mathcal{D}^{(\ell)\dagger}_{m,m'}(\gamma_{\mathcal{R}}) Y^{\ell *}_{m'}(\Omega_{\boldsymbol{k}'})\,, \tag{5b}$$

with $\varphi^-_{k,\ell,m} = \langle \ell, m | \varphi^-_{\boldsymbol{k}}(\boldsymbol{r})\rangle$. The theoretical challenge in describing continuum-electron interferometry stems from calculating matrix elements between continuum states. To this end, some schemes use regularization [43]. Here, we choose to converge the corresponding matrix elements with respect to the Gaussian basis. This approach may be converged systematically and takes advantage of the fact that the perturbed wave functions are semi-localized due to operation by the dipole (or other interaction) op-

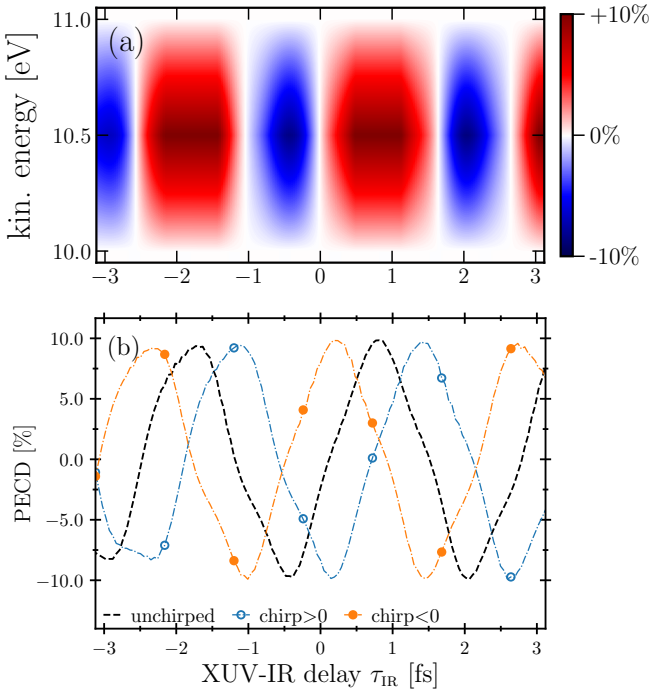

FIG. 2. Robustness of RABBITT-PECD: (a) PECD trace along the sideband $\mathcal{S}_{14}$ of Fig. 5(a) as a function of the XUV-IR time delay at the emission direction $\theta_{\boldsymbol{k}'} = 0°$ obtained with identical circular polarization states for the XUV and IR fields with polarization reversal as in Fig. 5(c). (b) Influence of the XUV comb delay dispersion on the sideband $\mathcal{S}_{14}$: positive and negative chirps merely shift the PECD value with respect to the unchirped case.

erator $\hat{\mu}$,

$$\psi^{(k)}(t) = (-i)^k \int_{t>t_1\cdots>t_k>t_0} e^{-i\hat{H}_0(t-t_1)}\,\hat{\mu}\,e^{-i\hat{H}_0(t_1-t_2)} \times \ldots \hat{\mu}\,e^{-i\hat{H}_0(t_k-t_0)}\,\psi(t_0)\;dt_1\ldots dt_k\,. \tag{6}$$

While each operation with $\hat{\mu}$ extends the range of the function, it is still local and representable by Gaussian functions, so long as they are converged. Calculations of occupied and unoccupied Hartree-Fock orbitals of the equilibrium geometry were obtained using the `MOLPRO` program package [44, 45] using the augmented correlation consistent basis set `aug-cc-pVQZ` [46]. Transition matrix elements to scattering states were obtained with the `ePolyScat` program package [47–49].

Starting with the usual RABBITT scheme depicted in Fig. 5(a), we first investigate the influence of the IR field on PECD. To this end, we optimize the IR pulse parameters (amplitude, duration and delay) for different polarization configurations of the XUV and IR pulses, with fixed IR frequency ($\omega_{IR} = \omega_0$) and fixed XUV parameters (10^{11}W/cm^2, 10 fs FWHM). The XUV pulse is defined by a synchronous frequency comb of odd-order harmonics ω_{11}, ω_{13} and ω_{15} as indicated in Fig.5(a) with flat spectral phase ($\tau_k = \tau_{k+1} = 0$). By taking the fundamental $\omega_0 = 1.5$ eV, XUV inner-shell and IR multiphoton contributions to the photoelectron spectra of interest are avoided, while simultaneously placing IR-excitation of vibrational modes far from resonance [50]. In the absence of the IR field, the XUV pulse induces the photoelectron spectrum shown in Fig. 5(b), with a maximum of PECD of 2% at a photoelectron kinetic energy of 6 eV. XUV-ionization in the presence of an IR pulse with optimized intensity (1.26×10^{12} W/cm^2) and time-delay (0.92 fs), results in a stronger dichroic effect with a maximum PECD of 10% at the sideband corresponding to a photoelectron kinetic energy of 10.5 eV, as shown in Fig. 5(c). Remarkably, the PECD obtained with the optimized IR pulse vanishes at the harmonics peaks.

The enhancement in the PECD due to the presence of the IR pulse, largest at the sideband $\mathcal{S}_{14}$ (10.5 eV), cf. Fig. 5(c), is obtained with circular polarization of both, XUV and IR pulses. The corresponding polarization reversal is indicated by the red (IR) and blue (XUV) arrows in Fig. 5(c). Removing the IR field and blue-shifting the XUV frequencies by 1.5eV to promote single-photon ionization at the energies corresponding to the sidebands (4.5, 7.5 and 10.5 eV) results in a significantly smaller PECD, cf. the Supplemental Material [51]. The decrease of the PECD at the $\mathcal{S}_{14}$ sideband when removing the IR field and blue-shifting the XUV excludes kinetic energy effects and confirms an interference effect as the main driver for the enhancement. Keeping the polarization of the XUV pulse fixed to an anticlockwise direction and inverting only that of the IR field results in a maximum PECD of 7% at 7.5 eV, and 5% at 10.5 eV. Such an approach may be valuable as the polarization of the IR fields is generally easier to manipulate. The strongest PECD values, however, are obtained under polarization reversal of both the XUV and IR fields. This suggests that contributions from bound-continuum and continuum-continuum transitions obtained with polarization reversal for both fields are combined to enhanced the overall PECD, as we will discuss in more detail below.

The extent to which the interferences are controlled by the relative delay between the IR and XUV fields is investigated in Fig. 6(a), showing the PECD trace centered around the sideband $\mathcal{S}_{14}$ of Fig. 5(a), at 10.5 eV, for the IR- and XUV-reversed polarization configurations displayed in Fig. 5(c). An oscillating behavior of the PECD as a function of the XUV-IR time delay is observed with alternating PECD sign. The pattern and oscillation period is sensitive to the relative polarization configuration of both fields as well as to the sideband position and IR pulse duration, cf. Supplemental Material. In particular, we find that the maximum achievable PECD increases for shorter IR durations and reaches a plateau as a function of the ratio of IR to XUV intensities (which occurs at a few percent). In all cases, the PECD exhibits an oscillatory behavior as function of the delay

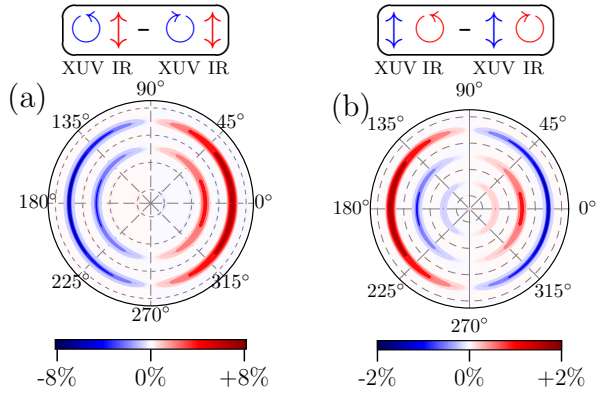

FIG. 3. Disentangling bound and continuum contributions to RABBITT-PECD by choice of the polarization configurations: (a) PECD obtained with circularly polarized XUV and linearly polarized IR pulses. (b) PECD obtained with linearly polarized XUV and circularly polarized IR pulses. Shown is the maximum PECD obtained for the respective optimal time delays. The dotted-gray lines in the polar plots indicate the harmonic peak positions $\mathcal{H}_{2q+1}$.

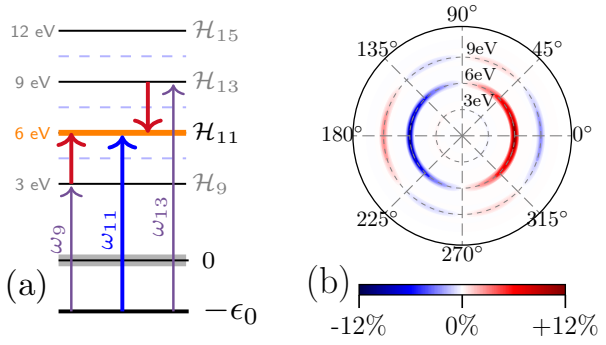

FIG. 4. (a) Modified RABBITT scheme for probing the kinetic energy dependence of PECD: Replacing the IR pulse by a visible field (with $\omega_{\mathrm{VIS}} = 2\omega_0$) results in interferences between even- and odd-parity pathways and controls PECD at the harmonic peaks instead of the sidebands. (b) Corresponding PECD to be compared to PECD without interference at the harmonic peaks (Fig. 5(b)) and to interference-enhanced PECD at the sidebands (Fig. 5(c)).

τ_{IR} for fixed IR amplitude and FHWM.

The PECD in Fig. 6(a) was obtained by assuming a flat spectral phase for the overall XUV comb, i.e., unchirped XUV harmonics. The RABBITT technique has exposed, however, the existence of a quadratic spectral phase for the plateau of high harmonic generation [29, 35, 36, 52, 53]. This has been interpreted as a temporal dispersion in the emission time of the group delay associated with each harmonic ω_{2q+1} [35, 36]. Consequently, the various XUV frequency components defining the comb are linearly delayed in time [35]. In Fig. 6(b) we investigate the extent to which such a delay dispersion affects the overall PECD signal. In detail, a positive chirp, corresponding to lower XUV harmonics preceding the higher ones, introduces a shift of the PECD peaks towards positive XUV-IR time-delays (blue line with empty circles) compared to the unchirped case (dotted-black line). Conversely, a negative chirp results in a shift towards negative time-delays (orange line with full circles). For a fixed delay, dispersion effects inherent to the high-order harmonic generation process may significantly affect the PECD strength. Remarkably, the chirped and unchirped XUV combs generate just delayed versions of the time-resolved PECD. This points to the robustness of the proposed interferometric scheme: If the XUV delay dispersion merely introduces a shift in the PECD oscillations, for an unknown chirp, the maximum achievable PECD can simply be retrieved by scanning the XUV-IR time-delay, cf. Fig. 6(b).

Modifying the polarization configurations allows us to harness the full potential of the interferometric scheme. To this end, we evaluate the PECD with left/right polarization reversal for the XUV field, keeping the IR polarization linear, as indicated by the arrows in Fig. 8(a). In the polarization configuration of Fig. 8(a), the role of the IR field is reduced to merely promoting interferences between two consecutive harmonic components of the photoelectron wave packet generated in single-photon ionization by the XUV comb. In this scenario, continuum-continuum transitions do not contribute to the PECD since the IR is linearly polarized. As before, the interferences can be controlled by the XUV-IR time delay, which for this configuration results in a maximum PECD of 8%, shown in Fig. 8(a), at a photoelectron kinetic energy of 10.5 eV. This has to be compared to the PECD of just 2% in the absence of the IR field at the same photoelectron energy, obtained with appropriately shifted XUV frequencies, cf. Supplemental Material.

The enhancement of the PECD highlights the role of interference between continuum states, even for a linearly polarized IR pulse. The difference between 10% in Fig. 5(c) and 8%, in Fig. 8(a) may be attributed to chiral effects directly in the continuum. To directly probe the chirality of the continuum states, we show in Fig. 8(b) the PECD for fixed linear polarization of the XUV field and circular polarization of the IR pulse. A maximum PECD of 2% is found at a photoelectron energy of 10.5 eV. The PECD of 2% shown in Fig. 8(b) is exclusively due to the continuum states as bound states do not contribute to the PECD for linearly polarized XUV fields.

Finally, we modify the standard RABBITT scheme depicted in Fig. 5(a) to promote interferences between harmonics separated by $\omega_{\mathrm{VIS}} = 2\omega_{\mathrm{IR}} = 3.0\,\mathrm{eV}$ as indicated in Fig. 7(a). Optimizing the visible pulse parameters (amplitude, FWHM, time delay) while keeping those of the XUV as in Fig. 5 and with the relative polarization configuration of Fig. 5(c), we obtain a maximum PECD of about 12% at a photoelectron kinetic energy of 6 eV shown in Fig. 7(b). Analogously to Fig. 6(b),

the magnitude of PECD oscillates as a function of the VIS-to-XUV time delay. The maximum PECD of 12% at 6 eV in Fig. 7(b) has to be compared to the PECD of 3% at 6 eV obtained with the XUV alone shown in Fig. 5(b). The significant enhancement in PECD compared to Fig. 5(b) can be attributed to the interfering pathways $\omega_9+2\omega_{\rm IR}$ and $\omega_{13}-2\omega_{\rm IR}$ depicted by the violet and red arrows in Fig. 7(a), which are absent in Fig.5(b). In fact, the single-photon ionization pathway represented by ω_{11} in Fig. 7(a) plays a minor role in the PECD enhancement: removing ω_{11} from the XUV comb results in maximum PECD of 10%. The main contribution to the PECD enhancement observed in Fig. 7 can thus be attributed to a two-photon pathway interference effect, determined by the pathways $\omega_9+2\omega_{\rm IR}$ and $\omega_{13}-2\omega_{\rm IR}$ interfering at 6 eV. Replacing the IR field ($\omega_0 = 1.5$ eV) that maximizes the PECD at the sidebands in Fig. 5(c) with a visible field ($\omega_0 = 3.0$ eV) as in Fig. 7 allows us to probe and exploit kinetic energy dependence effects. Both two-photon interferometric schemes discussed here result in an overall enhancement of the PECD compared to the XUV-only case. This attests to the ability of two-photon quantum pathway interferences to enhance PECD across the kinetic energy spectrum by exploiting continuum-continuum transitions with a minimum number of control parameters, and offers a complementary control protocol to schemes based on bound-state one- and two-photon quantum interference.

In conclusion, using CHBrClF as a chiral prototype, we have identified a robust scheme for the control of photoelectron circular dichroism in randomly oriented chiral molecules based on laser-assisted photoelectron wave packet interferometry. Control of PECD is achieved by manipulating interferences which can be controlled by means of the XUV-IR time delay. In striking contrast to multicolor phase control schemes [23] which are highly sensitive to the temporal coherence and require pulse shaping techniques which, while within experimental reach, are not yet practically accessible, the present control scheme considerably reduces the number of control parameters while simultaneously preserving the robustness with respect to the overall spectral phase. In this regard, we have analyzed the sensitivity of the PECD with respect to the inherent XUV group delay dispersion, and shown that the XUV comb delay dispersion simply introduces a shift in the PECD oscillations as a function of the XUV-IR time delay but does not affect the maximum PECD amplitude. It is thus sufficient to scan the XUV-IR time delay to retrieve the optimal delay for a specific dispersion of the consecutive odd-order harmonics contributing to the same sideband energy. We have also shown that by controlling the relative polarization between the XUV and IR pulses, the RABBITT technique can be exploited to probe the individual contributions of bound and continuum states to the PECD in a time-resolved manner. In this regard, experimental verification of RABBITT-PECD would confirm that PECD is largely due to the chiral potential experienced by the bound state electrons while continuum-state transitions contribute to a lesser extent. The continuum states, however, are critical to enhance PECD via interferences promoted by the IR field. Our work opens the way for robust control of PECD based on widely implemented laser-assisted photoelectron wave packet interferometry techniques with a minimum number of control parameters while disentangling the bound and continuum contributions to the PECD.

We acknowledge Chi-Hong Yuen for his contribution to implementing part of the code used in this work. The computing for this project was performed on the Beocat Research Cluster at Kansas State University, which is funded in part by NSF grants CNS-1006860, EPS-1006860, and EPS-0919443, ACI-1440548, CHE-1726332, and NIH P20GM113109, and used resources of the National Energy Research Scientific Computing Center (NERSC), a U.S. Department of Energy Office of Science User Facility operated under Contract No. DE-AC02-05CH11231 using NERSC award BES-ERCAP0024357. C. A. and L. G. were supported by the Chemical Sciences, Geosciences, and Biosciences Division, Office of Basic Energy Sciences, Office of Science, U.S. Department of Energy, under Grant No. DE-SC0022105. C. A. also acknowledges NSF Grant No. 2244539 for additional support during the summer of 2023. A. B. and C. P. K. acknowledge financial support from the Deutsche Forschungsgemeinschaft (CRC 1319).

SUPPLEMENTAL MATERIAL

We provide here: (i) convergence test calculations of the RABBITT-PECD as a function of the basis set used for the electronic structure calculations, (ii) calculations of PECD as a function of the full width at half maximum (FWHM) of the IR field, and (iii) the input file parameters for the electronic structure and scattering calculations. In accordance with the manuscript, the PECD values are given in percentage of the mean peak intensity of the photoelectron angular distribution (PAD). In accordance with the manuscript, the PECD values are given in percentage of the mean peak intensity of the photoelectron angular distribution (PAD).

Convergence tests

One-photon PECD

The results reported in the manuscript were obtained with the augmented correlation consistent basis sets `aug-cc-pVQZ` [54] to describe occupied and unoccupied Hartree-Fock orbitals. Figure 5 displays the one-photon

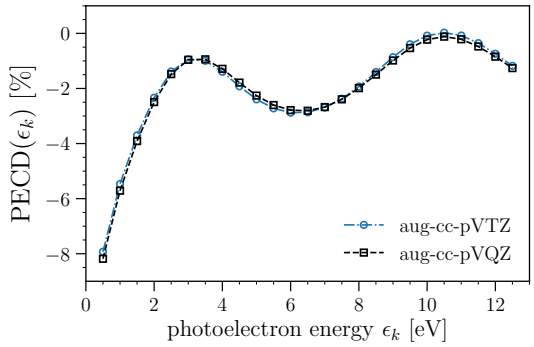

FIG. 5. One-photon PECD as a function of the photoelectron kinetic energy $\epsilon_k = \omega_{\mathrm{XUV}} - |\epsilon_0|$ obtained with the `aug-cc-pVTZ` and `aug-cc-pVQZ` basis set.

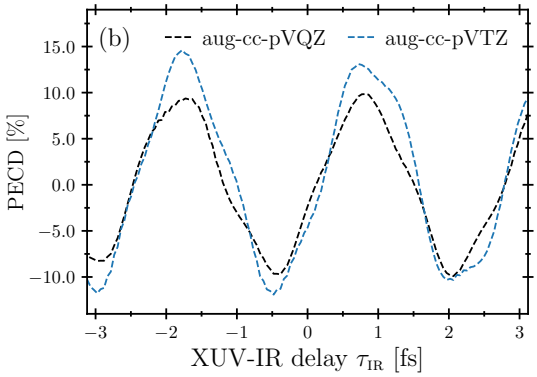

FIG. 6. Two-photon PECD as a function of XUV-IR delay obtained with the aug-cc-pVTZ and aug-cc-pVQZ basis sets. The PECD is given in percentage of the mean peak intensity of the PADs obtained with the polarization reversal configuration of Fig. 1(b) in the manuscript.

PECD as a function of the photoelectron kinetic energy obtained with the augmented correlation consistent basis `aug-cc-pVTZ` (circled blue-dashed lines) and the `aug-cc-pVQZ` basis (black-dashed lines). The ionizing field is defined by an isolated XUV comb of mean photon energy $\omega_{\mathrm{XUV}} = \epsilon_k + |\epsilon_0|$, with ϵ_k the photoelectron kinetic energy and ϵ_0 the HOMO energy obtained for each of these basis sets, with values of $-11.7062\,\mathrm{eV}$ and $-11.7007\,\mathrm{eV}$ at the equilibrium geometry for the `aug-cc-pVTZ` and `aug-cc-pVQZ` basis, respectively. The remaining XUV pulse parameters are fixed and correspond to those described in the manuscript. For both basis sets, the PECD is obtained with the polarization reversal corresponding to Fig. 1(b) in the manuscript. The IR field is absent. Overall, good agreement is obtained using both basis sets over the photoelectron energy range we have considered, which ranges from 0.5 eV to 12.5 eV. The asymptotic momentum components of the scattering states are truncated at `LmaxK`. For both basis sets, the PECD is found to converge within a precision below 0.1% for `LmaxK` = 20 for all photoelectron kinetic energies we have considered.

RABBITT-PECD

In our calculations, the final continuum states populated after absorption of an XUV and IR photon are obtained using the scattering formalism described in the manuscript. In contrast, the transient intermediate continuum states populated after XUV ionization are described by means of the highly-lying unoccupied Hartree-Fock orbitals obtained from electronic structure calculations (see discussion in the manuscript).

To check the sensitivity of the RABBITT-PECD on the high-lying orbitals representing the intermediate continuum states, we compare in Fig. 6 the RABBITT-PECD as a function of the XUV-IR time delay obtained with the augmented basis sets `aug-cc-pVQZ` and `aug-cc-pVTZ`. Black-dashed lines in Fig. 6 correspond to the RABBITT-PECD as a function of the XUV-IR time delay reported in Fig. 2(b) in the manuscript for the unchirped case (obtained with the `aug-cc-pVQZ` basis set). The blue-dashed lines in Fig. 6 corresponds to the time-resolved RABBIT-PECD obtained with the less accurate `aug-cc-pVTZ` basis set. While for the one-photon PECD in Fig. 5 both basis sets are in very good agreement, the two-photon PECD in Fig. 6 shows discrepancies between both basis sets.

One source of discrepancy stems from the fact that the `aug-cc-pVQZ` basis leads to a more energetically dense set of virtual Hartree-Fock orbitals. For `aug-cc-pVQZ`, the energy distribution increases quadratically for the lower virtual Hartree-Fock orbitals as a function of the orbital energy (analogously to the energy distribution of a particle in a box) compared to the `aug-cc-pVTZ` basis, which has a less dense and more oscillatory energy distribution. In either case, the virtual orbitals contributes coherently to the PECD within the bandwidth of the XUV and IR pulses and any difference in the description of these virtual states will affect the PECD at the sidebands. Regardless of these small differences, the oscillations as a function of the IR-XUV delay as well as the robustness with respect to XUV delay dispersion (chirp) persist independently of the choice of the basis.

Influence of the FWHM

The oscillations observed in Fig. 2 in the manuscript deviate from the standard RABBITT oscillations which follow a pure oscillatory behavior $\propto \cos(2\omega_{\mathrm{IR}}\tau_0 + \phi)$. The latter expression is obtained under the assumption that the IR field can be described by a cw field. Indeed, we find that constraining the FWHM of the IR pulse during optimization to larger values results in a delay-dependent

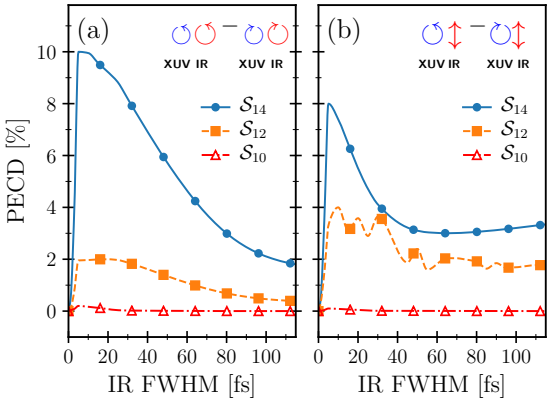

FIG. 7. Maximum PECD at sidebands $\mathcal{S}_{10}$ (4.5 eV), $\mathcal{S}_{12}$ (7.5 eV) and $\mathcal{S}_{14}$ (10.5 eV) as a function of the IR full-width at half maximum (FWHM) for the polarization configuration indicated by the blue (XUV) and red (IR) arrows in panels (a) and (b).

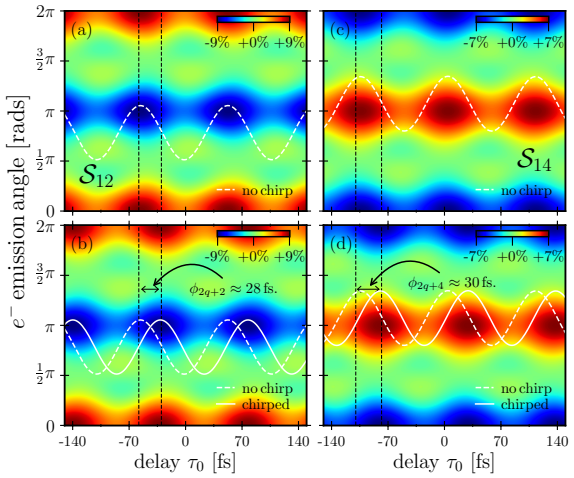

FIG. 8. (a) Maximum PECD at sideband $\mathcal{S}_{12}$ as a function of the azimuthal emission angle $\theta_{\boldsymbol{k}'}$ and time delay τ_0 for zero group dely dispersion ($\tau_{j+1} - \tau_j = 0$) of the XUV field. (b) same as (a) but including a positive chirp in the group delay dispersion of the XUV field comb as discussed in the manuscript. The spectral properties of the XUV components introduces a shift in the PECD value that can be retrived by shifting the XUV-IR time delay τ_0. Panels (c) and (d) shows the same property, for sideband $\mathcal{S}_{14}$. Note that the phase shift $\phi_{2(q+n)}$ relative to the unchirped case is sideband-dependent.

RABBITT-PECD described by the expected oscillatory behavior. However, the maximum PECD strength that can be obtained with longer IR pulses is weaker compared to the PECD obtained with shorter IR pulses. This can be seen in Fig. 7, which shows the maximum PECD achievable as a function of the FWHM for the XUV and IR polarization configurations indicated by the blue (XUV) and red (IR) arrows in panels (a) and (b). When the PECD is obtained upon polarization reversal of both XUV and IR pulses, the resulting PECD decreases monotonically as a function of the IR FWHM from its maximum value of 10%. On the other hand, when the IR is linearly polarized, the PECD decreases and reaches a plateau for the sidebands $\mathcal{S}_{12}$ (7.5 eV) and $\mathcal{S}_{14}$ (10.5 eV). The difference in magnitude between the PECD change over the consider FWHM values between both pulses counter-rotating in Fig. 7(a) and linearly polarized IR in Fig. 7(b) may be understood by considering that the XUV pulse contributes most of the PECD effect as discussed in the manuscript. The relative change in magnitude is not large, but the rest of the small effect can be attributed to the polarization of the IR.

Thus, apart from introducing deviations to the standard RABBITT oscillatory behavior, shorter IR pulses lead to a stronger dichroic effect. Pure oscillatory behavior $\propto \cos(2\omega_{\rm IR}\tau_0 + \phi)$ are restored for longer IR FWHM as shown in Fig. 8, showing the RABBITT oscillations (dotted-white lines) as a function of the photoemission angle (vertical axis) and the XUV-IR time delay (horizontal axis) at fixed photoelecton energies of 7.5 eV (a) and 10.5 eV (c) for the unchirped case, respectively. Panels (c) and (d) show the PECD trace obtained with a chirped XUV comb of odd-order harmonics. As for the shorter IR cases discussed in the manuscript, a group delay dispersion in the ionizing XUV field merely shifts the PECD values independently of IR pulse duration as shown in panels (b) and (d) in Fig. 8. This highlights the robustness of the proposed interferometric approach as the maximum PECD strength depends on the pulse duration and the XUV-to-IR time delay and avoids pulse shaping and control over the spectral properties of the PECD-inducing field.

Input file parameters

Input file parameters for MOLPRO

```
# MOLPRO Program package [44, 45] input file

***,CHFClBr gs
RCH= 1.088 ANG
RCCl= 1.745 ANG
RCBr= 1.928 ANG
RCF= 1.356 ANG
aHCF= 108.806 DEGREES
aHCCl= 108.5 DEGREES
aHCBr= 108.5 DEGREES
aFCCl= 109.93 DEGREES
aFCBr= 108.95 DEGREES
aClCBr= 112.09 DEGREES
geometry={
C1;
H1,C1,RCH;
Cl2,C1,RCCl,H1,aHCCl;}
Br3,C1,RCBr,H1,aHCBr,Cl2,aClCBr,1;
```

```
F4,C1,RCF,H1,aHCF,Cl2,aFCCl,-1;
}
basis=avqz
{rhf; wf,68,1,0;orbprint,40;}
optg;
put, molden, CHFClBr-avqz.molden;
```

Input file parameters for ePolyScat

```
# ePolyScat Program package [47, 48] input
file
# input file CHFClBr photoionization
#  and matrix elements calculation

#***,CHFClBr
LMax 30
EMax 20
EngForm
0 3
FegeEng 13.0
ScatEng .50
LMaxK 20
NoSym
InitSym 'A'
InitSpinDeg 1
OrbOccInit 2 2 2 2 2 2 2 2 2 2 2 2 2 2 2 2 2 2
2 2 2 2 2 2 2 2 2 2 2 2 2 2 2 2 2 2 2 2 2 2
OrbOcc 2 2 2 2 2 2 2 2 2 2 2 2 2 2 2 2 2 2 2 2
2 2 2 2 2 2 2 2 2 2 2 2 2 2 2 2 2 2 2 2 2 1
SpinDeg 1
TargSym 'A'
ScatContSym 'A'
ScatSym 'A'
TargSpinDeg 2
IPot 10.98

Convert 'chfclbr-avqz.molden''molden2012'
FileName 'MatrixElements''MatEle.idy''REWIND'
FileName 'DumpOut''DumpOut.idy''REWIND'
GetBlms
ExpOrb
GenFormPhIon
GetPot
DipoleOp
PhIon .50
DumpIdy 'MatEle.idy'.50
```

* Present Address: Department of Physics, University of Connecticut, Theoretical Atomic, Molecular and Optical Physics Center, Connecticut, 06269, USA

† lgreenman@phys.ksu.edu

[1] A. D. McNaught and A. D. McNaught, Compendium of chemical terminology, Vol. 1669 (Blackwell Science Oxford, 1997).
[2] B. Ritchie, Phys. Rev. A **13**, 1411 (1976).
[3] C. Lux, M. Wollenhaupt, T. Bolze, Q. Liang, J. Köhler, C. Sarpe, and T. Baumert, Angew. Chem. Int. Ed. **51**, 5001 (2012).
[4] C. Lux, M. Wollenhaupt, C. Sarpe, and T. Baumert, ChemPhysChem **16**, 115 (2015).
[5] C. Lux, A. Senftleben, C. Sarpe, M. Wollenhaupt, and T. Baumert, J. Phys. B **49**, 02LT01 (2016).
[6] A. Kastner, C. Lux, T. Ring, S. Züllighoven, C. Sarpe, A. Senftleben, and T. Baumert, ChemPhysChem **17**, 1119 (2016).
[7] A. Kastner, T. Ring, B. C. Krüger, G. B. Park, T. Schäfer, A. Senftleben, and T. Baumert, J. Chem. Phys. **147**, 013926 (2017).
[8] C. S. Lehmann, N. B. Ram, I. Powis, and M. H. M. Janssen, J. Chem. Phys. **139**, 234307 (2013).
[9] M. H. M. Janssen and I. Powis, Phys. Chem. Chem. Phys. **16**, 856 (2014).
[10] M. M. R. Fanood, N. B. Ram, C. S. Lehmann, I. Powis, and M. H. M. Janssen, Nature Commun. **6**, 7511 (2015).
[11] M. M. R. Fanood, M. H. M. Janssen, and I. Powis, Phys. Chem. Chem. Phys. **17**, 8614 (2015).
[12] R. Cireasa, A. E. Boguslavskiy, B. Pons, M. C. H. Wong, D. Descamps, S. Petit, H. Ruf, N. Thiré, A. Ferré, J. Suarez, J. Higuet, B. E. Schmidt, A. F. Alharbi, F. Légaré, V. Blanchet, B. Fabre, S. Patchkovskii, O. Smirnova, Y. Mairesse, and V. R. Bhardwaj, Nature Phys. **11**, 654–658 (2015).
[13] A. Comby, S. Beaulieu, M. Boggio-Pasqua, D. Descamps, F. Légaré, L. Nahon, S. Petit, B. Pons, B. Fabre, Y. Mairesse, and V. Blanchet, J. Phys. Chem. Lett. **7**, 4514 (2016).
[14] S. Beaulieu, A. Comby, B. Fabre, D. Descamps, A. Ferré, G. Garcia, R. Géneaux, F. Légaré, L. Nahon, S. Petit, T. Ruchon, B. Pons, V. Blanchet, and Y. Mairesse, Faraday Discuss. **194**, 325 (2016).
[15] S. Beaulieu, A. Ferré, R. Géneaux, R. Canonge, D. Descamps, B. Fabre, N. Fedorov, F. Légaré, S. Petit, T. Ruchon, V. Blanchet, Y. Mairesse, and B. Pons, New J. Phys. **18**, 102002 (2016).
[16] S. Beaulieu, A. Comby, A. Clergerie, J. Caillat, D. Descamps, N. Dudovich, B. Fabre, R. Géneaux, F. Légaré, S. Petit, B. Pons, G. Porat, T. Ruchon, R. Taïeb, V. Blanchet, and Y. Mairesse, Science **358**, 1288 (2017).
[17] S. Beaulieu, A. Comby, D. Descamps, B. Fabre, G. A. Garcia, R. Géneaux, A. G. Harvey, F. Légaré, Z. Masin, L. Nahon, A. F. Ordonez, S. Petit, B. Pons, Y. Mairesse, O. Smirnova, and V. Blanchet, Nature Phys. **14**, 484 (2018).
[18] J. Miles, D. Fernandes, A. Young, C. Bond, S. Crane, O. Ghafur, D. Townsend, J. Sá, and J. Greenwood, Analytica Chimica Acta **984**, 134 (2017).
[19] N. Böwering, T. Lischke, B. Schmidtke, N. Müller, T. Khalil, and U. Heinzmann, Phys. Rev. Lett. **86**, 1187 (2001).
[20] U. Hergenhahn, E. E. Rennie, O. Kugeler, S. Marburger, T. Lischke, I. Powis, and G. Garcia, The Journal of Chemical Physics **120**, 4553 (2004), https://doi.org/10.1063/1.1651474.

[21] P. V. Demekhin, A. N. Artemyev, A. Kastner, and T. Baumert, Phys. Rev. Lett. **121**, 253201 (2018).

[22] S. Rozen, A. Comby, E. Bloch, S. Beauvarlet, D. Descamps, B. Fabre, S. Petit, V. Blanchet, B. Pons, N. Dudovich, and Y. Mairesse, Phys. Rev. X **9**, 031004 (2019).

[23] R. E. Goetz, C. P. Koch, and L. Greenman, Phys. Rev. Lett. **122**, 013204 (2019).

[24] G. Hartmann, M. Ilchen, P. Schmidt, C. Küstner-Wetekam, C. Ozga, F. Scholz, J. Buck, F. Trinter, J. Viefhaus, A. Ehresmann, M. S. Schöffler, A. Knie, and P. V. Demekhin, Phys. Rev. Lett. **123**, 043202 (2019).

[25] P. M. Paul, E. S. Toma, P. Breger, G. Mullot, F. Augé, P. Balcou, H. G. Muller, and P. Agostini, Science **292**, 1689 (2001).

[26] H. Muller, Applied Physics B **74**, s17 (2002).

[27] T. Mazza, M. Ilchen, A. J. Rafipoor, C. Callegari, P. Finetti, O. Plekan, K. C. Prince, R. Richter, M. Danailov, A. Demidovich, et al., Nature communications **5**, 3648 (2014).

[28] S. Donsa, N. Douguet, J. Burgdörfer, I. Březinová, and L. Argenti, Phys. Rev. Lett. **123**, 133203 (2019).

[29] K. Klünder, J. M. Dahlström, M. Gisselbrecht, T. Fordell, M. Swoboda, D. Guénot, P. Johnsson, J. Caillat, J. Mauritsson, A. Maquet, R. Taïeb, and A. L'Huillier, Phys. Rev. Lett. **106**, 143002 (2011).

[30] M. Han, J.-B. Ji, T. Balčiūnas, K. Ueda, and H. J. Wörner, Nature Phys. (2022), 10.1038/s41567-022-01832-4.

[31] M. Han, J.-B. Ji, K. Ueda, and H. J. Wörner, Optica **10**, 1044 (2023).

[32] M. D. J. Waters, N. Ladda, A. Senftleben, V. Svoboda, M. Belozertsev, T. Baumert, and H. J. Wörner, Chem. Phys. Chem. **23** (2022), 10.1002/cphc.202200575.

[33] M. Pitzer, M. Kunitski, A. S. Johnson, T. Jahnke, H. Sann, F. Sturm, L. P. H. Schmidt, H. Schmidt-Böcking, R. Dörner, J. Stohner, J. Kiedrowski, M. Reggelin, S. Marquardt, A. Schießer, R. Berger, and M. S. Schöffler, Science **341**, 1096 (2013).

[34] K. Fehre, S. Eckart, M. Kunitski, C. Janke, D. Trabert, M. Hofmann, J. Rist, M. Weller, A. Hartung, L. P. H. Schmidt, T. Jahnke, H. Braun, T. Baumert, J. Stohner, P. V. Demekhin, M. S. Schöffler, and R. Dörner, Phys. Rev. Lett. **126**, 083201 (2021).

[35] S. Kazamias and P. Balcou, Phys. Rev. A **69**, 063416 (2004).

[36] Y. Mairesse, A. de Bohan, L. J. Frasinski, H. Merdji, L. C. Dinu, P. Monchicourt, P. Breger, M. Kovačev, R. Taïeb, B. Carré, H. G. Muller, P. Agostini, and P. Salières, Science **302**, 1540 (2003).

[37] I. Powis, The Journal of Chemical Physics **112**, 301 (2000).

[38] R. E. Goetz, C. P. Koch, and L. Greenman, J. Chem. Phys. **151**, 074106 (2019).

[39] PECD is given at fixed $\phi_{\boldsymbol{k}'} = \pi/2$, see e.g., Refs. [21], [23] and [38] for a detailed description of the detection geometry.

[40] C. W. McCurdy, D. A. Horner, and T. N. Rescigno, Phys. Rev. A **63**, 022711 (2001).

[41] M. Baertschy, T. N. Rescigno, and C. W. McCurdy, Phys. Rev. A **64**, 022709 (2001).

[42] R. R. Lucchese, G. Raseev, and V. McKoy, Phys. Rev. A **25**, 2572 (1982).

[43] N. Douguet, B. I. Schneider, and L. Argenti, Phys. Rev. A **98**, 023403 (2018).

[44] H.-J. Werner, P. J. Knowles, G. Knizia, F. R. Manby, M. Schütz, P. Celani, T. Korona, R. Lindh, A. Mitrushenkov, G. Rauhut, K. R. Shamasundar, T. B. Adler, R. D. Amos, A. Bernhardsson, A. Berning, D. L. Cooper, M. J. O. Deegan, A. J. Dobbyn, F. Eckert, E. Goll, C. H. l, A. Hesselmann, G. Hetzer, T. Hrenar, G. Jansen, C. Köppl, Y. Liu, A. W. Lloyd, R. A. Mata, A. J. May, S. J. McNicholas, W. Meyer, M. E. Mura, A. Nicklass, D. P. O'Neill, P. Palmieri, D. Peng, K. Pflüger, R. Pitzer, M. Reiher, T. Shiozaki, H. Stoll, A. J. Stone, R. Tarroni, T. Thorsteinsson, and M. Wang, "Molpro, version 2012.1, a package of ab initio programs," .

[45] H.-J. Werner, P. J. Knowles, G. Knizia, F. R. Manby, and M. Schütz, Wiley Interdisciplinary Reviews: Computational Molecular Science **2**, 242 (2012).

[46] R. A. Kendall, T. H. Dunning, and R. J. Harrison, The Journal of Chemical Physics **96**, 6796 (1992).

[47] F. A. Gianturco, R. R. Lucchese, and N. Sanna, J. Chem. Phys. **100**, 6464 (1994).

[48] A. P. P. Natalense and R. R. Lucchese, J. Chem. Phys. **111**, 5344 (1999).

[49] L. Greenman, R. R. Lucchese, and C. W. McCurdy, Phys. Rev. A **96**, 052706 (2017).

[50] M. Diem and D. F. Burow, The Journal of Chemical Physics **64**, 5179 (1976).

[51] Supplemental Material.

[52] K. Varjú, Y. Mairesse, P. Agostini, P. Breger, B. Carré, L. J. Frasinski, E. Gustafsson, P. Johnsson, J. Mauritsson, H. Merdji, P. Monchicourt, A. L'Huillier, and P. Salières, Phys. Rev. Lett. **95**, 243901 (2005).

[53] M. Isinger, D. Busto, S. Mikaelsson, S. Zhong, C. Guo, P. Salières, C. Arnold, A. L'Huillier, and M. Gisselbrecht, Phil. Trans. R. Soc. A. **377**, 20170475 (2019).

[54] R. A. Kendall, T. H. Dunning Jr., and R. J. Harrison, J. Chem. Phys. **96**, 6796 (1992).